Journal of Power Sources 357 (2017) 77–86

Contents lists available at ScienceDirect

Journal of Power Sources

journal homepage: www.elsevier.com/locate/jpowsour

Multi-scale 3D investigations of a commercial 18650 Li-ion battery with correlative electron- and X-ray microscopy

Jeff Gelb [a, *], Donal P. Finegan [b], Dan J.L. Brett [b], Paul R. Shearing [b]

[a] Carl Zeiss X-Ray Microscopy, Pleasanton, CA, USA
[b] Electrochemical Innovation Lab, Department of Chemical Engineering, University College London, Torrington Place, London, WC1E 7JE, UK

HIGHLIGHTS

- A commercial 18650 battery was studied using correlative microscopy (XRM & SEM).
- A virtual model of the battery microstructure and composition was constructed.
- Porosity, tortuosity, and effective diffusion coefficient were quantified.
- The Bruggeman exponent was determined, using standard image processing routines.

GRAPHICAL ABSTRACT

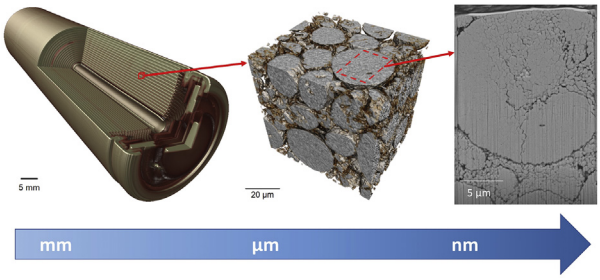

ARTICLE INFO

Article history:
Received 6 February 2017
Received in revised form
15 April 2017
Accepted 28 April 2017

Keywords:
18650
Characterization
X-ray microscopy
Scanning-electron microscopy
Correlative microscopy
Tortuosity

ABSTRACT

In the present study, a commercial 18650 Li-ion cylindrical cell is investigated with non-destructive 3D X-ray microscopy across a range of length scales, beginning with a survey of the entire cell and non-destructively enlarging a smaller section. Active materials are extracted from a disassembled cell and imaging performed using a combination of sub-micron X-ray microscopy and 2D scanning-electron microscopy, which point toward the need for multi-scale analysis in order to accurately characterize the cell. Furthermore, a small section is physically isolated for 3D nano-scale X-ray microscopy, which provides a measurement of porosity and enables the effective diffusivity and 3-dimensional tortuosities to be calculated via computer simulation. Finally, the 3D X-ray microscopy data is loaded into a correlative microscopy environment, where a representative sub-surface region is identified and, subsequently, analyzed using electron microscopy and energy-dispersive X-ray spectroscopy. The results of this study elucidate the microstructural characteristics and potential degradation mechanisms of a commercial NCA battery and, further, establish a technique for extracting the Bruggeman exponent for a real-world microstructure using correlative microscopy.

1. Introduction

There is considerable and growing research interest in Li-ion batteries driven largely by an increase in dependence on energy storage solutions, for applications ranging from mobile electronics to stationary power supplies and electric vehicles [1–3]. In the coming years, increasingly demanding applications from mW to MW, will require advanced Li-ion batteries to operate under extremes of temperature, rate, and pressure. Li-ion batteries are expected to deliver high performance, over long lifetimes, at a reduced cost as compared to existing solutions. With growing dependence on Li-ion technologies, in particular due to the

* Corresponding author. 4385 Hopyard Rd., Pleasanton, CA, 94588, USA.
E-mail address: jeff.gelb@zeiss.com (J. Gelb).

http://dx.doi.org/10.1016/j.jpowsour.2017.04.102
0378-7753/

growing popularity of hybrid- and fully-electric vehicles [2], it is of paramount importance to understand how batteries perform, age, and degrade under real-world conditions [4,5]. Recent high profile failures have emphasized the need to better understand these processes [6–8].

There are a range of Li-ion battery architectures commercially available, such as pouch, prismatic, and spiral wound cells; by far the most common geometry is the 18650 cell, which has found diverse applications from consumer electronics [9] to aerospace equipment [10] and automotive power trains [11]. While the chemistry within these cells may vary, there are common components across most available commercial cells: the functional cell comprises two porous electrodes, electrically isolated by a porous separator material, the three layers are spiral wound into the 18650 casing, and various safety components including positive temperature coefficient (PTC) devices, pressure relief valves, and current interrupt devices are connected and crimped into the casing [9].

In recent years, there has been growing interest in the relationship between the complex and often heterogeneous microstructure of the porous electrodes and the electrochemical performance of the device. It is hypothesized that microscopic heterogeneities and defects [12] within these materials may act as nucleation points for macroscopic failures and, consequently, there is a need to understand these material microstructures in greater detail [13]. For example, the expansion and contraction of active electrode materials can cause SEI and particle fracture on the micro scale [14,15], whereas the same chemo-mechanical forces can result in severe delamination and electrical isolation of the bulk electrode [5,16]. The authors and others have led work over the past 5 years in the application of X-ray tomography to explore these materials both ex-situ [14,17–21] and in-situ [14,15,22,23]. Additional work using tomography and radiography to characterize cell architecture during failure [22] and post mortem [24,25] as well as to understand the role of safety features [26–28] help to build a comprehensive understanding of the role of each component in driving device degradation and failure. This work is complemented by extensive investigations using SEM [29,30]and FIB-SEM [31], TEM [32], XRD [33], and AFM [34], as well as multi-scale investigations that demonstrate the need for the integration of various imaging instruments to characterize batteries [35,36].

Collectively, these studies highlight the importance of understanding the multi-scale nature of Li-ion batteries from the pack to the particle levels [25,36]; it is essential that researchers identify appropriate length scale(s) for understanding key mechanisms that affect the performance and reliability of cells [36]. Macro-scale features, such as assembly issues, may affect the mechanical and chemical stability, while micro-scale features, such as particle assembly and porosity/tortuosity may affect the overall capacity and operational properties. Furthermore, nano-scale features, such as SEI growth, dendrite formation, and intraparticle cracks may affect the long-term safety and reliability of a battery, but must be understood in the context of other features [37]. There are many aspects of the battery's microstructure that may dictate its performance, but it is important to simultaneously consider features ranging from the macro-to the micro- and nano-scales [35,36].

This multi-scale challenge can be effectively addressed by correlative lab-based imaging instrumentation, using optical, electron and ion beam microscopy and 3D micro- and nano-XRM [25]. Using this correlative imaging approach, each modality is used for its unique strength: for example, the tunable magnification of SEM in 2D and switchable energy dispersive X-ray spectrometry for chemical analysis, along with the non-destructive 3D and 4D imaging capabilities of XRM [38,39].

Recent progress in 3D imaging techniques have indicated deviations between theoretical models and actual formations in battery microstructures and, in so doing, have grown in popularity. Historically, microstructure investigations have hinged on stereological techniques, but the results are often inconclusive [40]. Recent 3D imaging studies have illustrated the anisotropic, non-ideal nature of a “typical” Li-ion battery electrode microstructure, which has demonstrated that models based purely on single 2D images may not be sufficient to accurately describe the transport properties of electrode materials [41]. Using 2D stereological approaches alone may, thus, lead to inaccurate representations of the microstructures leading to ultimate errors in characterization; these issues can be mitigated by employing 3D imaging approaches, such as XRM and FIB-SEM [40].

The present study demonstrates, for the first time, the application of both XRM and SEM to probe a single commercial 18650 Li-ion battery across multiple length scales, starting with the full cell and moving all the way down to examining sub-particle features. X-ray techniques afford the unique capability for non-destructive imaging, allowing the same sample to be imaged multiple times under different conditions. Using this advantage, the present study thus paves the way for future investigations in which 18650 batteries may be studied before, during, and after aging cycles, in a so-called “4D” imaging experiment. This information forms a foundation for several such future imaging studies and illustrates the unique abilities of modern microscopy techniques to aid in the advancement of Li-ion battery research and development.

2. Materials and methods

2.1. Materials preparation

Commercially sourced Panasonic NCR 18650-B cylindrical cells were used for the present study. These high energy density cells contain a nickel-cobalt-aluminum oxide (NCA) positive electrode and have demonstrated applications for mobile electronics and electric vehicles [42].

2.2. X-ray microscopy

X-ray microscopy (XRM) was used to non-destructively collect 3D volumetric data on the specimens and survey them before any dismantling. XRM, discussed extensively elsewhere [35,38,43–45], uses the X-ray computed tomography (CT) approach to collect 3D images of specimen interiors by collecting a series of projection X-ray radiographs at various viewing angles (achieved by rotating the specimen and exposing it to the X-ray beam). The resulting projection images were subsequently reconstructed using a Feldcamp-Davis-Kress (FDK) or filtered back projection (FBP) algorithm (the former for micron-to sub-micron imaging, and the latter for nano-scale imaging) [46], and the 3D datasets produced by this process were rendered and analyzed for porosity using ORS Visual Si Advanced (Object Research Systems, Montreal, QB, Canada) [38,44]. Further simulation studies were performed using GeoDict (Math2Market, Gmbh, Kaiserslautern, Germany) [47], which computed effective diffusivity [48,49], tortuosity [50], and, by means of morphological manipulation, a Bruggeman coefficient for the specimen under study.

Initial investigations were performed using a ZEISS Xradia 520 Versa X-ray microscope (Carl Zeiss X-ray Microscopy, Pleasanton, CA, USA), equipped with a 0.4 × objective lens to provide a 3D isotropic voxel size of 22 μm across the entire imaging volume. This allowed the entire width of the 18650 cylindrical cell to be captured in a single field of view in ca. 1 h, after which further imaging was performed along the vertical axis to cover the entire length of the cylindrical cell. The resulting five datasets were then stitched

together using the automated stitching routine in the commercial XRM software, producing a 3D volume covering the 18650 cell in its entirety. The 520 Versa submicron XRM system provides the capability to non-destructively (i.e., without sectioning) isolate smaller regions of interest for higher-resolution analysis, due to a unique optics-based design [38]. This "Scout & Zoom" technique [38,43,51] was thus employed on the larger volume to non-destructively probe the inner structure of the battery, using a 4 × objective lens magnification for a voxel size of 1.8 μm.

2.3. Correlative microscopy: Nano-XRM to SEM-EDS

For further, higher resolution imaging, the specimens were dismantled and unrolled in an argon glove box, to verify the 3D imaging results and prepare isolated specimens for higher resolution analysis. The battery was discharged over a 5 Ω resistance for 2 days until the voltage read 0 V. A pipe cutter was used to open the steel casing and the interior spiral wound layers were carefully removed. After carefully unrolling the electrode layers, the negative electrode, positive electrode, and separator were isolated from each other, washed with dimethyl carbonate (DMC) to remove any residual electrolyte or Li salts, and then left to dry for several days [42].

Subsequent imaging of the individual layers was carried out using several techniques, including submicron scale XRM, scanning electron microscopy (SEM), nanoscale XRM, focused-ion beam scanning electron microscopy (FIB-SEM), and energy dispersive spectroscopy (EDS). A 1 mm × 1 mm section was cut from the positive electrode foil using a razor blade, to prepare the specimen for correlative XRM-SEM imaging. The ZEISS Xradia 520 Versa XRM was used to image the electrode coupon with a 20 × objective, providing a voxel size of 350 nm. The specimen was then transferred to the Zeiss Sigma FE-SEM, where magnification ranges from 100 × to over 10k × where sequentially employed in order to probe the multi-scale nature of the microstructure. As a result of this analysis, the electrode samples were prepared for nano-scale 3D imaging by trimming them to a point (using a fresh surgical razor blade) and peeling away the current collector from the region of interest in order to maximize X-ray throughput. Real-time optical inspection was used for this procedure, during which no large-scale defects were observed, thus it was concluded that the separation process did not affect the microstructure of the intended region of interest. A ZEISS Xradia 810 Ultra was then used to provide 3D images with 130 nm voxel resolution on the specimens, using a 5.4 keV quasi-monochromatic imaging system operating in absorption contrast mode [52]. Finally, the specimens were passed into the ZEISS Auriga FIB-SEM system outfitted with an Oxford Instruments X-MaxN 150 EDS spectrometer. Using the ZEISS Atlas 5 correlative software interface, a representative region of interest (ROI) was identified from the submicron XRM data and the FIB instructed to cross-section at this location. High-resolution 2D SEM micrographs were collected in the identified ROI to visualize the nanoscale structure, and correlative EDS maps were collected with peaks fit around the Ni, Co, Al, and O edges to elucidate the specimen composition within a single secondary particle.

The present study utilized a variety of imaging techniques in order to complete the multi-scale analysis. Table 1 summarizes the various imaging instruments applied to this study, including submicron XRM, nanoscale XRM, FE-SEM, and FIB-SEM, along with the corresponding voxel sizes for the 3D XRM measurements.

Table 1
Listing of the various imaging techniques used in this study and the corresponding voxel size (3D XRM), pixel size (FIB-SEM), or magnification (FE-SEM), as appropriate.

Technique	Voxel Size/Pixel Size/Magnification
Submicron XRM – 520 Versa	22 μm
Submicron XRM – 520 Versa	1.8 μm
Submicron XRM – 520 Versa	0.35 μm
FE-SEM – Sigma	100 × - 10,000 ×
Nanoscale XRM – 810 Ultra	0.13 μm
FIB-SEM – Auriga	0.01 nm

3. Results & discussion

The initial large-scale survey of the intact 18650 enabled an initial non-destructive inspection of the specimen to identify any large-scale features. Fig. 1a shows the segmented 3D reconstruction, in which the inner layers of the electrode assembly can be seen clearly against the steel casing, central mandrel, and crimp components. Using the non-destructive Scout & Zoom procedure of the submicron XRM instrument [38,43,51], a smaller region from the center was arbitrarily selected for higher resolution imaging. Adjusting the objective lenses to provide a voxel size of 1.8 μm, this higher resolution inspection enabled a more detailed view of the active layers within the packaged 18650 cell, the results of which are shown in Fig. 1b and c.

The initial surveys with low-resolution XRM showed the general structure of the battery, enabling an initial observation of the cell assembly to be made. Different layers of the spiral wound cell were clearly distinguished from each other, helpful for general orientation in the higher-resolution investigation. This low-resolution approach is helpful for large-scale investigations, such as searching for bulk defects or inspecting the complex assembly within the top cap, but in the present study no such defects were located. Nevertheless, in the present study the large-volume overview allowed a completely non-destructive view into the battery's interior, which helped to establish a baseline as to whether or not there were obvious defects in the battery as manufactured.

By continuing to higher resolution with non-destructive XRM, it was demonstrated that single-micron resolution may be achieved inside the battery casing. At this scale, the difference between electrode layers, such as active materials and current collecting foils, was achieved, and any smaller-scale defects may be observed. This has the important distinction of being completely non-invasive and may be performed without opening the housing of the battery. Thus, at this length scale, it may be possible to study the origin of microstructure defects as a function of charge cycling, thermal treatment, or other real-world conditions potentially leading to failure/capacity fade [19].

While XRM as an imaging technique is, by nature, non-destructive, the imaging results may be affected by artifacts introduced by specimens that are significantly larger (>10 ×) than the microscope's field of view. In order to circumvent this issue, while also preparing specimens that were suitable for nano-scale XRM and FIB-SEM, the battery was opened, unrolled, and dried, to enable extraction of a much smaller specimen (ca. 1 mm × 1 mm). The positive electrode layer specimen was imaged in 3D using a voxel size of 350 nm on the submicron-scale XRM, sampling a large volume of material while preserving a voxel size small enough to capture the structural features within the layers. Results from this scan are shown in Fig. 2a, where the particle assembly and bulk porosity were clearly observed. This result also showed several cracks and bulk defects, which were suspected to be introduced during the dismantling/unrolling. By applying a threshold-based segmentation to this dataset, the pore networks were virtually extracted and analyzed on a slice-by-slice basis. Fig. 2b shows the results of the slice-by-slice porosity analysis. Several oscillations were observed in the slice-wise analysis, which are believed to indicate the packing order of the particles, suggesting quasi-

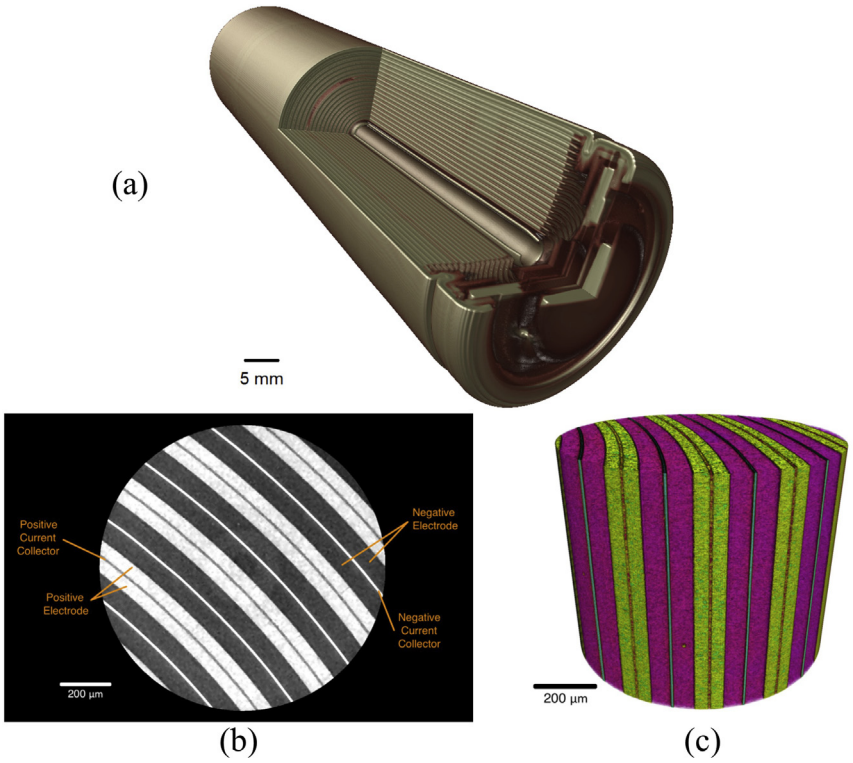

Fig. 1. (a) A 3D image of the entire 18650 battery cell was collected over several fields of view, which were subsequently stitched together to produce this dataset. This X-ray micrograph reveals the spiral would cell architecture, inner mandrel, and cell safety devices. (b) Optically enlarging a smaller region from the center of the 18650 battery cell revealed finer details of the layers in the spiral winding, and examining the virtual slices allowed identification and inspection of the different layers. (c) The virtual slices were assembled into a 3D volume, rendered here for the purposes of visualization. The yellow layers represent the positive electrode and the magenta layers represent the negative electrode, each with their respective current collectors sandwiched between electrode layers. In these scans, it was not possible to distinguish the separator (presumed polymer) from negative electrode (presumed graphite), due to low-energy X-ray attenuation by the steel casing and metallic foils. (For interpretation of the references to colour in this figure legend, the reader is referred to the web version of this article.)

spherical particles of reasonably uniform size. These results indicated that the average porosity was ~9% for each layer of active material, which was lower than expectations for a percolating pore system – this was believed to point toward the need for higher resolution for accurate analysis, which was performed in subsequent experiments.

To check the specimen morphology with multi-scale resolution, SEM micrographs of the positive electrode specimen were collected at various magnifications through the submicron- and nano scales. Fig. 3a shows a correlative XRM micrograph, while Fig. 3b shows the results of increasing magnification on the SEM. The higher magnification micrographs revealed a fine structure to both the particles and pores, with particles ca. 5 μm in size and pores in the hundreds of nanometers. This suggested that higher XRM resolution was needed to accurately characterize the electrode specimen, which was subsequently performed using a nanoscale XRM.

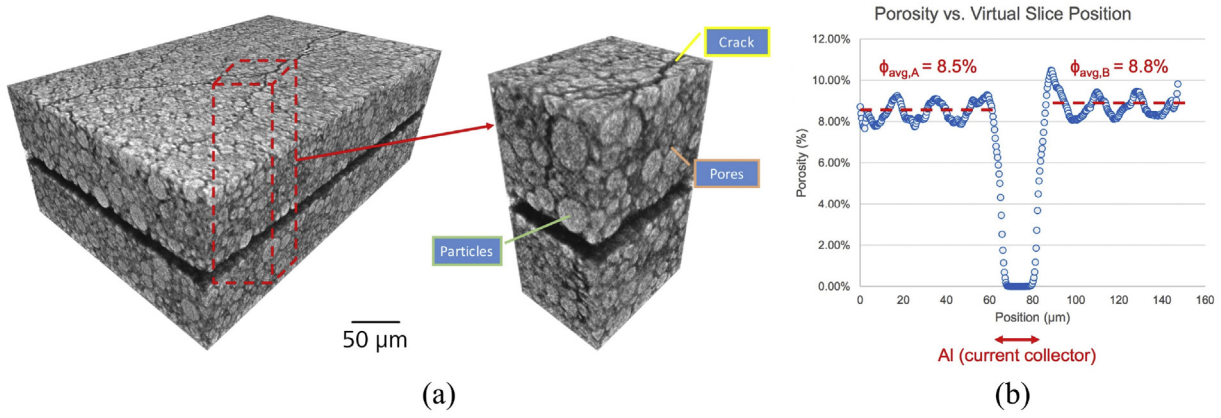

Fig. 2. (a) 3D volume rendering of the positive electrode layer, showing the particles, pores, and cracks/defects throughout the specimen thickness. b) Areal porosity computed for each virtual slice through the 3D volume, separated by the outer side (A) and inner side (B) of the rolled structure. Note that the slicewise analysis captured some regions near the current collector interface where nonuniformities in the current collector foil surface produced combined partial counts of current collector and electrode porosity. These are simply artifacts of the data analysis and can be seen as a multi-micron thick region of porosity gradient at each electrode-current collector interface.

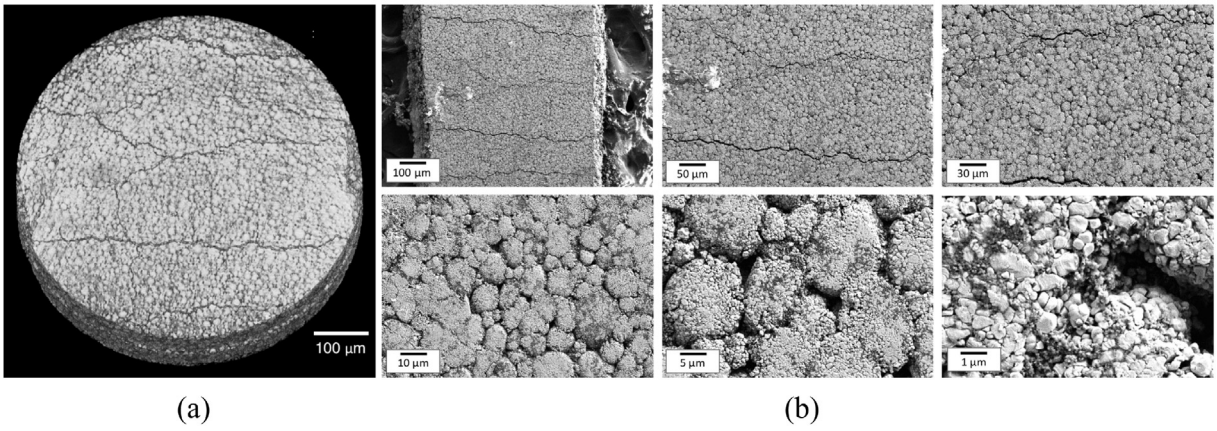

Fig. 3. (a) X-ray micrograph to be used in the correlative microscopy workflow. (b) Increasing SEM magnification reveals a fine structure of the positive electrode material, which points toward the need for higher resolution for an accurate multi-scale 3D characterization. At the length scale of submicron XRM, the particles and pores could be distinguished, but the complex microstructure of the particles themselves clearly requires nano-scale imaging.

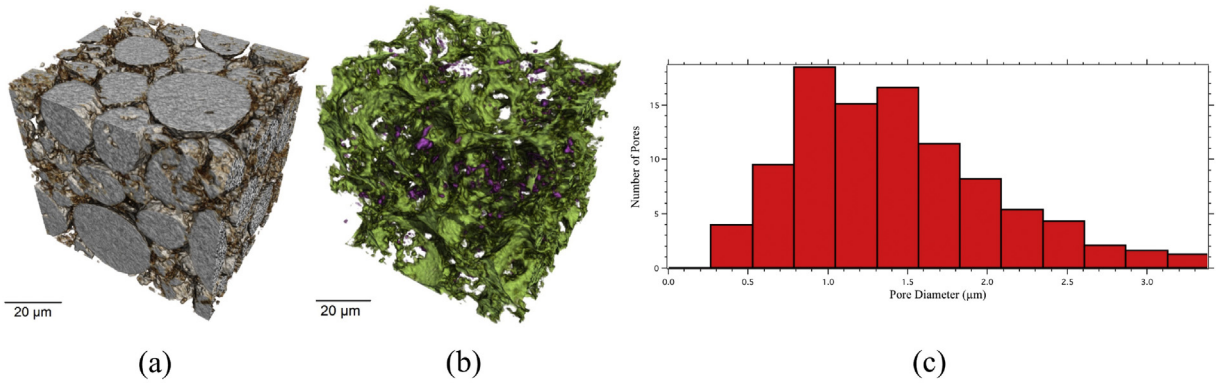

Fig. 4. (a) Nano-scale XRM performed on the positive electrode layer show (b) some isolated voids within the particles, as well as cracks within the particles connecting to the pore network. (c) Pore size distribution performed on the nanoscale XRM results, confirming the nanoscale nature of much of the porosity. The pore sizes are reported based on the method of inscribing ellipsoids to a separated version of the segmented pore network, with larger connected networks split at the constriction points (pore throats).

From the SEM micrographs, the multi-length scale nature of the specimen was clearly observed (as a 2D analog to prior studies, e.g. Ref. [36]). At low magnifications, the bulk particle assembly was visible, helpful for identifying "pristine" regions versus regions that showed defects. As the magnification was increased, the individual particles became clearer, as did the cracks between particles and pores visible along the surface of the material. Moving to the highest magnification on the SEM showed the bound primary particles making up the active particles, as well as the spacing between the primary particles.

To probe the fine structure of the particles and pores, the sample was imaged in 3D using the higher resolution provided by the nanoscale XRM. The smaller voxel size of 130 nm allowed for pore-scale resolution to be achieved, additionally showing cracks within the single particles, as shown in Fig. 4a. Some cracks were isolated within single particles and disconnected from the main pore network, while others were found to be connected to a percolation pathway. While the former likely represent fabrication defects within the particles, the latter produce longer electrochemically active surface areas and may represent sites where failures could ultimately nucleate [41]. By applying a segmentation to this dataset, the percolating pore pathways could be digitally separated from the isolated voids, as shown in Fig. 4b, yielding a measurement of 14.4% total porosity and 13.9% connected porosity. This represented a substantial increase in the porosity measurements by moving from submicron to nanoscale imaging resolution, which confirmed the need for nano-scale imaging in the 3D microstructure analysis. At this scale, however, still the aggregations of primary particles forming the active electrode clusters cannot be clearly distinguished; in order to achieve the spatial resolution needed for this characterization, a correlative microscopy technique bridging from XRM to SEM should be employed.

The nano-scale 3D XRM results were loaded into the GeoDICT software for further analysis using a variety of simulation routines. First, the percolating pore pathway was measured, illustrating a typical transport pathway within the pore network identified from this dataset. The pores were then analyzed for their 3D diameter distribution, as shown in Fig. 4c. From this result, it was clear that many pores within this specimen existed in the nanoscale regime, further supporting the application of multi-scale analysis ranging into the nanoscale for these material systems.

Next, a diffusion simulation [47–49] was performed in order to extract the effective diffusivity tensor and tortuosity in each of the three spatial dimensions, numerically describing the transport through the pore network. The solver was set up to simulate Laplacian diffusion (Kn $\ll$ 1) on the pore network with periodic boundary conditions, constrained to impose a concentration of 1 mol/m^3 at the inlet and 0 mol/m^3 at the outlet. The results yielded a 3D rendering of the concentration gradient, as shown in Fig. 5, as well as a numerical effective diffusivity tensor, as presented in

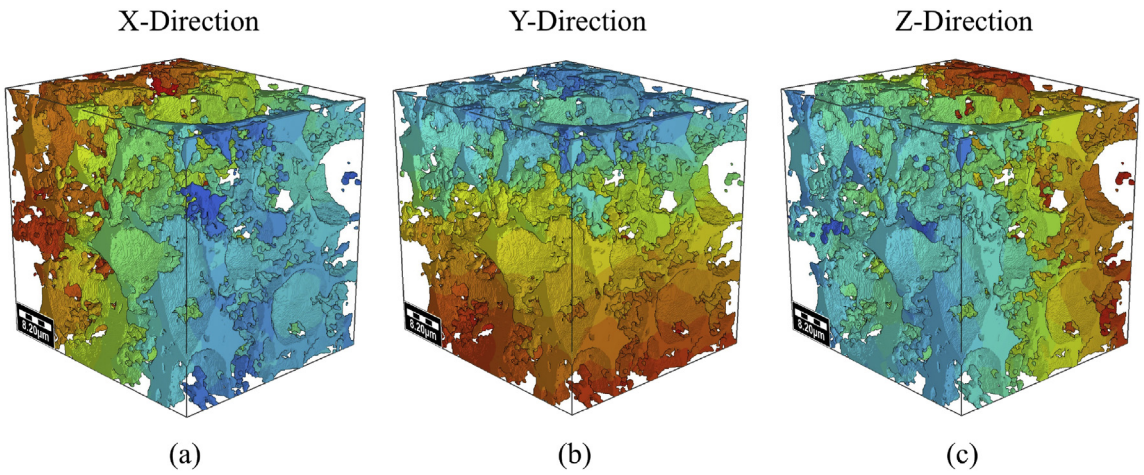

Fig. 5. Concentration gradients shown in 3D based on effective diffusivity simulations within the pore network. The diffusivities are shown as performed in the (a) X-, (b) Y-, and (c) Z-directions.

Table 2
Effective diffusivity for the nano-scale XRM volume, based on numerical simulation.

	X	Y	Z
X	**2.47**	0.09	−0.06
Y	0.09	**2.55**	0.03
Z	−0.06	0.03	**2.30**

Table 3
Directional tortuosities from the effective diffusivity simulation.

Tortuosity (X)	2.38
Tortuosity (Y)	2.34
Tortuosity (Z)	2.46

Table 2. These results were then arithmetically converted to tortuosity in each direction using the simulation software, the results of which are shown in Table 3.

Following the image analysis, the behavior of the pore network with Li^+ intercalation was explored based on simulated changes to the active particles. In its operating conditions (i.e., charging & discharging), the active particles expand as Li^+ intercalate and contract as the ions diffuse back out of the particles. This expansion process may be simulated in virtual space by use of a morphological dilation operation, which causes a 3D expansion of a virtual material by a specified number of voxels in all three dimensions. Using the binarized, segmented dataset to seed a model of the particle assembly, a dilation operation with kernel size of 1 voxel (130 nm) was applied in a sequential manner. The particle dilation caused a corresponding reduction in the pore volume, and the effective diffusivity/tortuosity was calculated after each dilation step. This resulted in a change in 3D concentration gradient, as illustrated in Fig. 6. As observed in the nano-XRM data (e.g., Fig. 4a), the particle sizes for the NCA material range from ca. 5–15 μm; thus, a single-voxel dilation of 130 nm corresponds to a particle expansion on the order of ~1%. This is in agreement with previously-reported lattice expansions of ~1% in a typical discharge cycle of an NCA-based Li-ion 18650 battery [53]. Thus, it was concluded that single-voxel dilations were a reasonable approach for simulating the microstructure's response to a discharge process.

Examining the decrease in porosity and relating the new porosity to the new tortuosity after each step permitted examination of the relationship between the two quantities for this specimen. By performing this analysis in all three directions, a tortuosity vs. porosity plot was ascertained, as shown in Fig. 7. This was accomplished by fitting the data to the well-established power law relationship:

$$\tau = \varepsilon^{-\beta}$$

where τ is the tortuosity, ε the porosity, and β the Bruggeman exponent [54,55]. While the value of β is commonly-assumed to be 0.5, recently this relationship has come under scrutiny due to the various limitations inherent in its definition [15,56,57]. An assumption of 0.5 as the value for β introduces additional assumptions about the homogeneity of microstructure, when, in practice, the microstructure of a typical battery electrode is highly inhomogeneous [41,57]. Thus, it is perhaps unsurprising that the fitted values for the Bruggeman exponent in each of the three spatial directions (X, Y, and Z) deviates from 0.5, as summarized numerically in Table 4.

It should be noted that, in a real-world battery, the particles would expand and potentially introduce internal stresses that could cause the particles to migrate away from each other. In the model presented here, the simulation does not account for particle motion and simply “fuses” particles together when the dilation introduces overlap. Thus, this approach represents a simplistic view into the microstructure evolution processes and is intended to introduce the concept of geometrical simulations on 3D data. There is ample room to make the simulation approach more sophisticated to account for the real-world effects that occur during discharge, but a full treatment of such processes is beyond the scope of the present investigation and, instead, reserved for future work.

While the SEM data illustrated the multi-scale nature of the material, the studies were intrinsically limited to 2D information, which prevented any studies of 3D porosity without the use of destructive serial-sectioning. The use of nano-scale XRM addressed that issue by non-destructively revealing the inter-particle pore network, as well as sub-particle defects (e.g. voids that were not connected to the outside). Separating the connected and disconnected pores allowed the extraction of an ionic transport pathway, which was essential for performing a diffusion simulation along the pore pathways to obtain the 3D tortuosity values [41]. Examining the effective diffusivity results, the off-diagonal tensor elements were insignificant compared to the diagonals, which indicates a negligible interaction between the directions of tortuosity. Thus, it was concluded that the transport pathway was spatially isotropic.

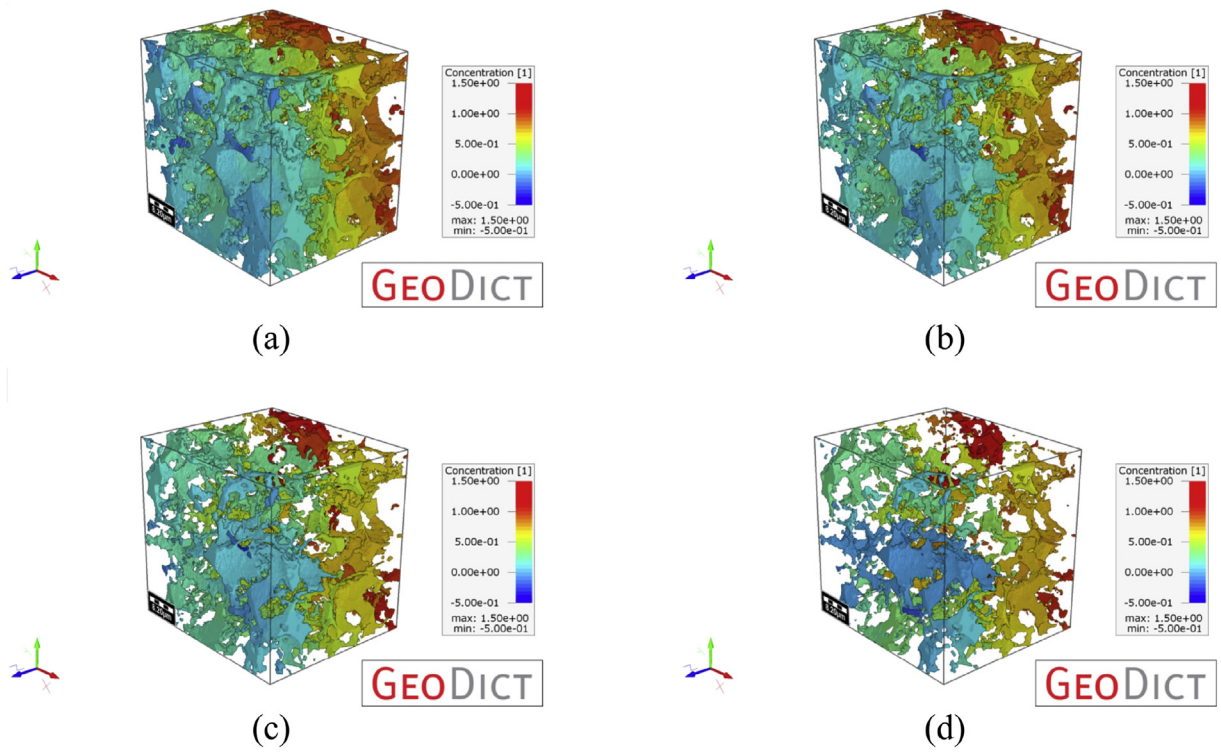

Fig. 6. Sequential particle dilation and corresponding change in 3D concentration gradient due to the change in effective diffusivity. (a) Initial data; (b) after 1 voxel dilation (130 nm); (c) after 2 voxels dilation (260 nm); (d) after 3 voxels dilation (390 nm). The Z direction only is shown here for the purposes of illustration.

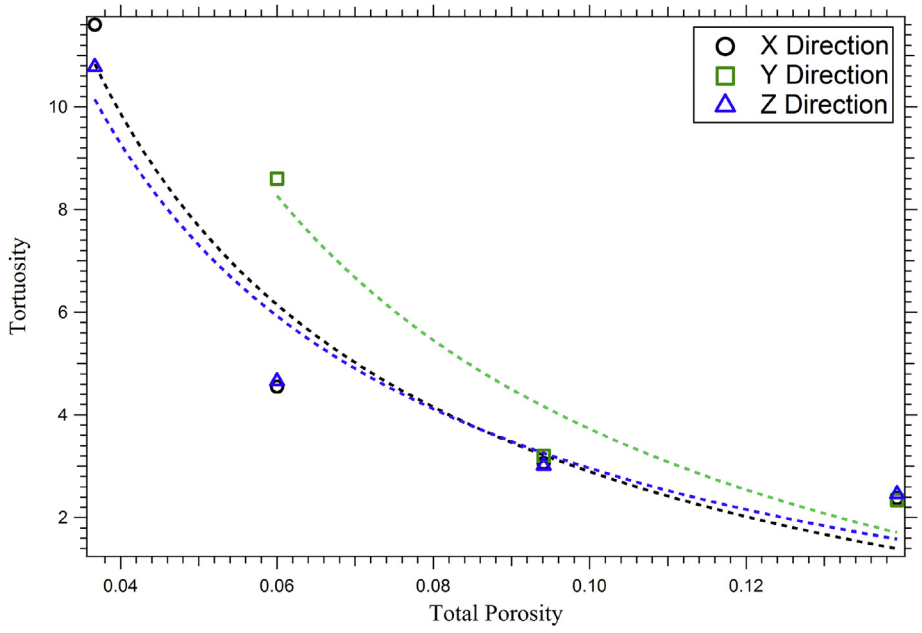

Fig. 7. Relationship of tortuosity to total porosity for the X, Y, and Z directions of simulated diffusion.

Table 4
Bruggeman exponent quantified for the positive electrode extracted from the 18650 and imaged with nanoscale XRM.

Direction	Bruggeman Exponent
X	0.81
Y	0.90
Z	0.78

This is more clearly shown by the tortuosity numbers, which exhibited minimal variations between the x-, y-, and z directions. The isotropy of tortuosity further suggested the quasi-spherical nature of the electrode particles [55], yielding additional information about the manufacturing and corresponding function of the cell. The deviation of the calculated Bruggeman exponent from the assumed value of 0.5 indicate a polydispersity in the particle size

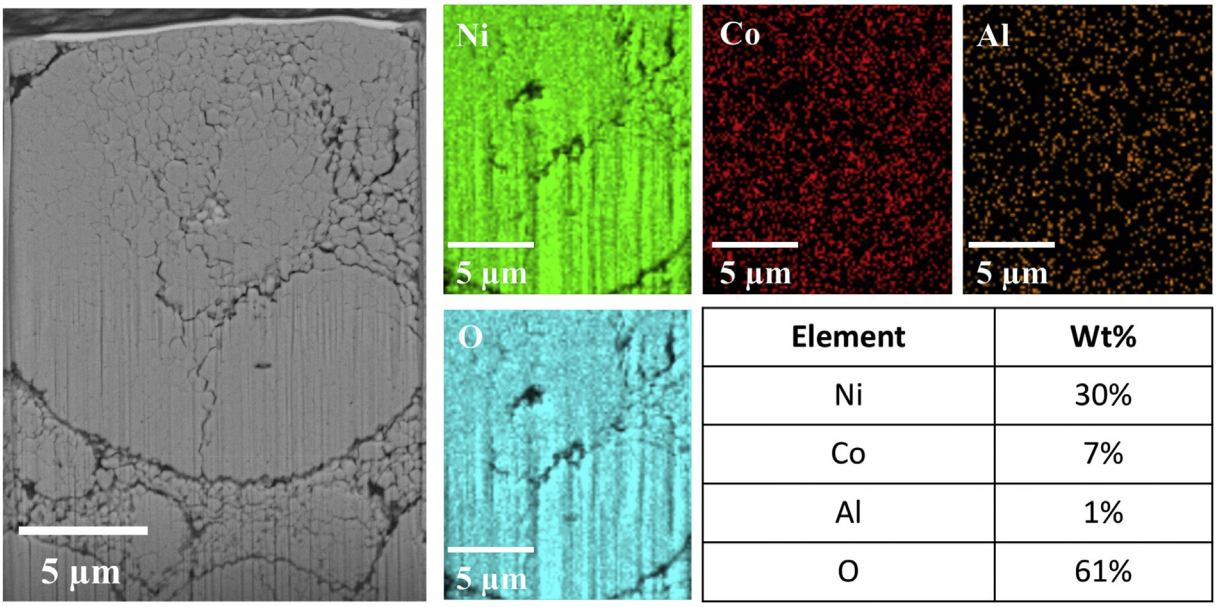

Element	Wt%
Ni	30%
Co	7%
Al	1%
O	61%

Fig. 8. (left) SEM micrograph of the targeted region of interest, identified via correlative microscopy with XRM. The results show several microstructural features, such as cracks, voids, and a particle boundary. (Right) Corresponding EDS map for this region, revealing the spatial distribution of the Ni, Co, Al, and O elements (and their corresponding weight percentages).

Table 5
Summary of relevant data produced by each technique in the multi-scale correlative study.

Technique	Length Scale	Data Output
Submicron XRM – 520 Versa	10s-100 s µm	• Defect mapping • ROI identification
Submicron XRM – 520 Versa	1-10 µm	• Layer identification • Defect isolation
Submicron XRM – 520 Versa	0.7 µm	• Bulk porosity • Particle-scale information
FE-SEM – Sigma	10 nm–10 µm	• Multi-scale 2D analysis of large areas
Nanoscale XRM – 810 Ultra	150 nm–10 s µm	• Porosity • Pore size distribution • Tortuosity/effective diffusivity
FIB-SEM-EDS – Auriga	10 nm	• High-resolution 2D/3D analysis • Targeted chemical analysis

distribution [56] and a value of ~0.8 is within the range of what may be expected from a commercial battery material when the complexity of tortuosity is considered [58].

In order to extend these investigations to an even finer length scale, the specimen was placed into a ZEISS Auriga FIB-SEM, which allows targeted regions of interest to be examined through focused ion beam cross-sectioning and SEM imaging of the region of interest. The XRM data was imported into the correlative microscopy workspace of Atlas 5 (Fibics, Inc., Ottawa, ON, Canada) and overlaid on an SEM micrograph of the top surface. Using a manually-assisted image registration routine, the datasets were aligned to each other to co-register the X-ray and electron microscopy images. A representative region of interest was visually identified within the XRM volume, which appeared to accurately depict the general specimen microstructure. This region of interest was selected below the surface of the specimen to reduce the influence of any surface cracks and was chosen to contained a particle-particle boundary as well as substantial greyscale texturing. This region was cross-sectioned with the FIB and imaged with the SEM, the results are shown in Fig. 8. Using an Oxford Instruments XMaxN-150 energy dispersive X-ray spectrometer (EDS), the local chemistry was mapped and fit to a composition of Ni-Co-Al-O, which was correlated to the SEM micrograph in Fig. 8.

Extending the SEM-XRM investigations to the ~10 nm length scale with targeted (correlative) FIB cross-sectioning demonstrated a novel approach to microstructure evaluation. While the XRM results provided sufficient resolution to identify many of the pores, from this correlative study it was clear that there was an additional length scale of information that could not be captured by XRM alone. By mapping out the local chemistry, it was observed that the particle under observation contained a typical NCA composition in a uniform blend, which allows the single particles to be treated as uniform compounds in future simulations (e.g., electrical, ionic, and thermal conductivity). The correlative approach using the Atlas 5 interface was critical for making this successful, as it required the XRM data for FIB guidance and navigation to a representative region of interest. Furthermore, this allows the SEM and EDS data to be easily populated back into the XRM data, for a more robust, integrated multi-scale representation of the specimen microstructure. The results of all techniques, when put together into a multi-scale, correlative analysis procedure as in the present study, are summarized in Table 5.

Further work combining XRM, SEM, and FIB-SEM-EDS results with other techniques, such as electrochemical impedance

spectroscopy (EIS) and thermal imaging, is thus within the realm of possibility. Combining imaging and simulation results with those from analytical approaches could help explain, for example, the exact cause of capacity fade, the reactions of cells to extreme (e.g., high temperature) environments, and, more generally, the origins of failure. Furthermore, using the non-destructive nature of X-ray imaging, future studies may focus on the evolution of Li-ion battery microstructures at the relevant length scale(s) of interest, probing, for example, the response of the structures to aging, impact, or thermal treatment.

4. Conclusion

A commercial 18650 Li-ion battery has been examined across several length scales, in both 2D and 3D, utilizing scanning-electron and X-ray microscopy, coupled with focused ion beam milling and energy dispersive X-ray spectroscopy. The battery was initially surveyed with low spatial resolution in 3D, which revealed the bulk assembly and allowed for the identification of any large-scale defects. A non-destructive optical magnification was then employed with the XRM system, showing the finer details within the active layers. Depackaging and imaging the battery with both 2D SEM and 3D XRM showed features across the micron-to nanometer scales, which was applied to both the positive electrode and negative electrode layers individually. Small sections of both the positive electrode and negative electrode were extracted for nano-scale XRM, revealing the fine nature of the pores and a separation between connected (transport) and disconnected (isolated) porosity. Through image segmentation and model generation, a simulation approach was used to compute the effective diffusion coefficient and tortuosity in each direction. Correlative microscopy from XRM to FIB-SEM-EDS revealed the nano-scale structure as well as the local composition of the electrode.

The results of this study highlight the different types of information achievable at each length scale and correlative microscopy is demonstrated as a viable means to present a detailed description of the chemistry and structure cell materials from the nm to mm. Using a combination of imaging modalities in both 2D and 3D paired with modeling and simulation approaches enables unique insight into battery cell geometry and electrode structure, providing a novel characterization framework for commercial battery products.

Acknowledgments

The authors gratefully acknowledge the financial support of the EPSRC ELEVATE (EP/M009394/1), Manifest (EP/N032888/1) and AMorpheuS (EP/N001583/1) programmes for sponsoring the battery research of DB and PRS, as well as technical support from Dr. Lorenz Lechner of Carl Zeiss X-ray Microscopy (Pleasanton, CA, USA). The authors also wish to thank Object Research Systems (Montreal, QB, Canada) for advice pertaining to visualization and Math2Market for their support in the 3D data analysis. Finally, the authors acknowledge Dr. Steve Harris (Lawrence Berkeley National Laboratory) and Dr. Melanie McNeil (San Jose State University) for many engaging discussions related to this research.

References

[1] J.M. Tarascon, M. Armand, Issues and challenges facing rechargeable lithium batteries, Nature 414 (15 November 2001) 359–367.
[2] B. Scrosati, B. Scrosati, J. Garche, J. Garche, Lithium batteries: status, prospects and future, J. Power Sources 195 (2010) 2419–2430, http://dx.doi.org/10.1016/j.jpowsour.2009.11.048.
[3] V. Etacheri, R. Marom, R. Elazari, G. Salitra, D. Aurbach, Challenges in the development of advanced Li-ion batteries: a review, Energy Environ. Sci. 4 (2011) 3243–3262, http://dx.doi.org/10.1039/c1ee01598b.
[4] A. Barré, A. Barré, undefined author, B. Deguilhem, undefined author, B. Deguilhem, et al., A review on lithium-ion battery ageing mechanisms and estimations for automotive applications, J. Power Sources 241 (2013) 680–689, http://dx.doi.org/10.1016/j.jpowsour.2013.05.040.
[5] D.P. Finegan, E. Tudisco, M. Scheel, J.B. Robinson, O.O. Taiwo, D.S. Eastwood, et al., Quantifying bulk electrode strain and material displacement within lithium batteries via high-speed operando tomography and digital volume correlation, Adv. Sci. 3 (2015) 1500332, http://dx.doi.org/10.1002/advs.201500332.
[6] Samsung, Galaxy Note7 Safety Recall and Exchange Program, 2016. http://www.samsung.com/us/note7recall/.
[7] Dreamliner, Boeing 787 Planes Grounded on Safety Fears, British Broadcasting Company News, 2013. http://www.bbc.com/news/business-21054089.
[8] Tesla Says Car Fire Started in Battery, 2013. http://wheels.blogs.nytimes.com/2013/10/02/highway-fire-of-tesla-model-s-included-its-lithium-battery/?ref=automobiles&_r=1.
[9] J.B. Goodenough, K.-S. Park, The Li-Ion rechargeable battery: a perspective, J. Am. Chem. Soc. 135 (2013) 1167–1176, http://dx.doi.org/10.1021/ja3091438.
[10] S. Yayathi, W. Walker, D. Doughty, H. Ardebili, Energy distributions exhibited during thermal runaway of commercial lithium ion batteries used for human spaceflight applications, J. Power Sources 329 (2016) 197–206, http://dx.doi.org/10.1016/j.jpowsour.2016.08.078.
[11] E.J. Cairns, P. Albertus, Batteries for electric and hybrid-electric vehicles, Annu. Rev. Chem. Biomol. Eng. 1 (2010) 299–320, http://dx.doi.org/10.1146/annurev-chembioeng-073009-100942.
[12] E. Darcy, Screening Li-ion batteries for internal shorts, J. Power Sources 174 (2007) 575–578, http://dx.doi.org/10.1016/j.jpowsour.2007.06.245.
[13] S.J. Harris, P. Lu, Effects of inhomogeneities—nanoscale to mesoscale—on the durability of Li-Ion batteries, J. Phys. Chem. C 117 (2013) 6481–6492, http://dx.doi.org/10.1021/jp311431z.
[14] J.M. Paz-Garcia, O.O. Taiwo, E. Tudisco, D.P. Finegan, P.R. Shearing, D.J.L. Brett, et al., 4D analysis of the microstructural evolution of Si-based electrodes during lithiation: time-lapse X-ray imaging and digital volume correlation, J. Power Sources 320 (2016) 196–203, http://dx.doi.org/10.1016/j.jpowsour.2016.04.076.
[15] M. Ebner, F. Marone, M. Stampanoni, V. Wood, Visualization and quantification of electrochemical and mechanical degradation in Li ion batteries, Science 342 (2013) 716–720, http://dx.doi.org/10.1126/science.1241882.
[16] J.B. Siegel, A.G. Stefanopoulou, P. Hagans, Y. Ding, D. Gorsich, Expansion of lithium ion pouch cell batteries: observations from neutron imaging, J. Electrochem. Soc. 160 (2013) A1031–A1038, http://dx.doi.org/10.1149/2.011308jes.
[17] P.R. Shearing, L.E. Howard, P.S. Jørgensen, N.P. Brandon, S.J. Harris, Characterization of the 3-dimensional microstructure of a graphite negative electrode from a Li-ion battery, Electrochem. Commun. 12 (2010) 374–377, http://dx.doi.org/10.1016/j.elecom.2009.12.038.
[18] P.R. Shearing, R.S. Bradley, J. Gelb, S.N. Lee, A. Atkinson, P.J. Withers, et al., Using synchrotron x-ray nano-CT to characterize SOFC electrode microstructures in three-dimensions at operating temperature, Electrochem. Solid-State Lett. 14 (2011), http://dx.doi.org/10.1149/1.3615824, 1177–B124.
[19] D.S. Eastwood, V. Yufit, J. Gelb, A. Gu, R.S. Bradley, S.J. Harris, et al., Lithiation-Induced dilation mapping in a lithium-ion battery electrode by 3D x-ray microscopy and digital volume correlation, Adv. Energy Mater 4 (2014) 1–7, http://dx.doi.org/10.1002/aenm.201300506.
[20] O.O. Taiwo, D.P. Finegan, J. Gelb, C. Holzner, D.J.L. Brett, P.R. Shearing, The use of contrast enhancement techniques in X-ray imaging of lithium–ion battery electrodes, Chem. Eng. Sci. 154 (2016) 27–33, http://dx.doi.org/10.1016/j.ces.2016.04.023.
[21] M. Ebner, F. Geldmacher, F. Marone, M. Stampanoni, V. Wood, X-ray tomography of porous, transition metal oxide based lithium ion battery electrodes, Adv. Energy Mater 3 (2013) 845–850, http://dx.doi.org/10.1002/aenm.201200932.
[22] D.P. Finegan, M. Scheel, J.B. Robinson, B. Tjaden, In-operando high-speed tomography of lithium-ion batteries during thermal runaway, Nature 6 (2015) 6924, http://dx.doi.org/10.1038/ncomms7924.
[23] S.-C. Chao, Y.-C. Yen, Y.-F. Song, Y.-M. Chen, H.-C. Wu, N.-L. Wu, A study on the interior microstructures of working Sn particle electrode of Li-ion batteries by in situ X-ray transmission microscopy, Electrochem. Commun. 12 (2010) 234–237, http://dx.doi.org/10.1016/j.elecom.2009.12.002.
[24] V. Yufit, P. Shearing, R.W. Hamilton, P.D. Lee, M. Wu, N.P. Brandon, Investigation of lithium-ion polymer battery cell failure using X-ray computed tomography, Electrochem. Commun. 13 (2011) 1–13, http://dx.doi.org/10.1016/j.elecom.2011.03.022.
[25] D.P. Finegan, M. Scheel, J.B. Robinson, B. Tjaden, M. Di Michiel, G. Hinds, et al., Investigating lithium-ion battery materials during overcharge-induced thermal runaway: an operando and multi-scale X-ray CT study, Phys. Chem. Chem. Phys. (2016), http://dx.doi.org/10.1039/c6cp04251a.
[26] D.P. Finegan, S.J. Cooper, B. Tjaden, O.O. Taiwo, J. Gelb, G. Hinds, et al., Characterising the structural properties of polymer separators for lithium-ion batteries in 3D using phase contrast X-ray microscopy, J. Power Sources 333 (2016) 184–192, http://dx.doi.org/10.1016/j.jpowsour.2016.09.132.
[27] M.F. Lagadec, M. Ebner, R. Zahn, V. Wood, Communication—technique for visualization and quantification of lithium-ion battery separator

microstructure, J. Electrochem. Soc. 163 (2016) A992–A994, http://dx.doi.org/10.1149/2.0811606jes.
[28] J.B. Robinson, J.A. Darr, D.S. Eastwood, G. Hinds, P.D. Lee, P.R. Shearing, et al., Non-uniform temperature distribution in Li-ion batteries during discharge - a combined thermal imaging, X-ray micro-tomography and electrochemical impedance approach, J. Power Sources 252 (2014) 51–57, http://dx.doi.org/10.1016/j.jpowsour.2013.11.059.
[29] S.T. Boles, A. Sedlmayr, O. Kraft, R. Mönig, In situ cycling and mechanical testing of silicon nanowire anodes for lithium-ion battery applications, Appl. Phys. Lett. 100 (2012) 243901–243904, http://dx.doi.org/10.1063/1.4729145.
[30] M. Müller, L. Pfaffmann, S. Jaiser, M. Baunach, V. Trouillet, F. Scheiba, et al., Investigation of binder distribution in graphite anodes for lithium-ion batteries, J. Power Sources 340 (2017) 1–5, http://dx.doi.org/10.1016/j.jpowsour.2016.11.051.
[31] M. Biton, V. Yufit, F. Tariq, M. Kishimoto, N. Brandon, Enhanced imaging of lithium ion battery electrode materials, J. Electrochem. Soc. 164 (2016) A6032–A6038, http://dx.doi.org/10.1149/2.0061701jes.
[32] X.H. Liu, J.W. Wang, S. Huang, F. Fan, X. Huang, Y. Liu, et al., In Situ Atomic-scale Imaging of Electrochemical Lithiation in Silicon, 2012, pp. 1–8, http://dx.doi.org/10.1038/nnano.2012.170.
[33] K.J. Rhodes, R. Meisner, M. Kirkham, N. Dudney, C. Daniel, In situ XRD of thin film tin electrodes for lithium ion batteries, J. Electrochem. Soc. 159 (2012) A294–A299, http://dx.doi.org/10.1149/2.077203jes.
[34] N. Balke, S. Jesse, A.N. Morozovska, E. Eliseev, D.W. Chung, Y. Kim, et al., Nanoscale Mapping of Ion Diffusion in a Lithium-ion Battery Cathode, 2010, pp. 1–6, http://dx.doi.org/10.1038/nnano.2010.174.
[35] P.R. Shearing, D.S. Eastwood, R.S. Bradley, J. Gelb, S. Cooper, F. Tariq, et al., Exploring electrochemical devices using X-ray microscopy: 3D microstructure of batteries and fuel cells, Microsc. Analysis (2013) 1–4.
[36] P.R. Shearing, N.P. Brandon, J. Gelb, R. Bradley, P.J. Withers, A.J. Marquis, et al., Multi length scale microstructural investigations of a commercially available Li-Ion battery electrode, J. Electrochem. Soc. 159 (2012) A1023–A1027, http://dx.doi.org/10.1149/2.053207jes.
[37] L. Lu, X. Han, J. Li, J. Hua, M. Ouyang, A review on the key issues for lithium-ion battery management in electric vehicles, J. Power Sources 226 (2013) 272–288, http://dx.doi.org/10.1016/j.jpowsour.2012.10.060.
[38] A.P. Merkle, J. Gelb, The ascent of 3D x-ray microscopy in the laboratory, Micros. Today 21 (2013) 10–15, http://dx.doi.org/10.1017/S1551929513000060.
[39] A. Merkle, L. Lechner, A. Steinbach, J. Gelb, M. Kienle, Automated correlative tomography using xrm and fib-sem to span length scales and modalities in 3d materials, Microsc. Analysis (2014) S10–S13.
[40] O.O. Taiwo, D.P. Finegan, D.S. Eastwood, J.L. Fife, L.D. Brown, J.A. Darr, et al., Comparison of three-dimensional analysis and stereological techniques for quantifying lithium-ion battery electrode microstructures, J. Microsc. 263 (2016) 280–292, http://dx.doi.org/10.1111/jmi.12389.
[41] D. Kehrwald, P.R. Shearing, N.P. Brandon, P.K. Sinha, S.J. Harris, Local tortuosity inhomogeneities in a lithium battery composite electrode, J. Electrochem. Soc. 158 (2011) A1393–A1397, http://dx.doi.org/10.1149/2.079112jes.
[42] T. Hayashi, J. Okada, E. Toda, R. Kuzuo, Degradation mechanism of LiNi0.82Co0.15Al0.03O2 positive electrodes of a lithium-ion battery by a long-term cycling test, J. Electrochem. Soc. 161 (2014) A1007–A1011, http://dx.doi.org/10.1149/2.056406jes.
[43] M. Feser, J. Gelb, H. Chang, H. Cui, F. Duewer, S.H. Lau, et al., Sub-micron resolution CT for failure analysis and process development, Meas. Sci. Technol. 19 (2008) 094001–094008, http://dx.doi.org/10.1088/0957-0233/19/9/094001.
[44] J. Gelb, Functionality to failure: materials engineering in the 4th dimension, Am&P 170 (2012) 1–5.
[45] P.R. Shearing, Y. Wu, S.J. Harris, N.P. Brandon, In Situ X-Ray Spectroscopy and Imaging of Battery Materials, The Electrochemical Society Interface, 2011, pp. 43–47.
[46] S.R. Stock, MicroComputed Tomography, CRC Press, 2008.
[47] MathMarket, Gmbh, GeoDict, (n.d.). http://www.geodict.com (Accessed 16 August 2016).
[48] A. Wiegmann, A. Zemitis, Ej-HEAT: a Fast Explicit Jump Harmonic Averaging Solver for the Effective Heat Conductivity of Composite Materials, 2006.
[49] J. Becker, C. Wieser, S. Fell, K. Steiner, A multi-scale approach to material modeling of fuel cell diffusion media, Int. J. Heat Mass Transf. 54 (2011) 1360–1368, http://dx.doi.org/10.1016/j.ijheatmasstransfer.2010.12.003.
[50] N. Epstein, On tortuosity and the tortuosity factor in flow and diffusion through porous media, Chem. Eng. Sci. 44 (1989) 777–779.
[51] T.L. Burnett, S.A. McDonald, A. Gholinia, R. Geurts, M. Janus, T. Slater, et al., Correlative tomography, Sci. Rep. 4 (2014) 1–6, http://dx.doi.org/10.1038/srep04711.
[52] A. Tkachuk, F. Duewer, H. Cui, M. Feser, S. Wang, W. Yun, X-ray computed tomography in Zernike phase contrast mode at 8 keV with 50-nm resolution using Cu rotating anode X-ray source, Z. Für Kristallogr. 222 (2007) 1–6, http://dx.doi.org/10.1524/zkri.2007.222.11.650.
[53] C.-K. Lin, Y. Ren, K. Amine, Y. Qin, Z. Chen, In situ high-energy X-ray diffraction to study overcharge abuse of 18650-size lithium-ion battery, J. Power Sources 230 (2013) 32–37, http://dx.doi.org/10.1016/j.jpowsour.2012.12.032.
[54] V. Bruggeman, Berechnung verschiedener physikalischer Konstanten von heterogenen Substanzen. I. Dielektrizitätskonstanten und Leitfähigkeiten der Mischkörper aus isotropen Substanzen, Ann. Der Phys. 416 (1935) 636–664, http://dx.doi.org/10.1002/andp.19354160705.
[55] M. Ebner, D.-W. Chung, R.E. Garcia, V. Wood, Tortuosity Anisotropy Lithium-Ion Battery Electrodes 4 (2013), http://dx.doi.org/10.1002/aenm.201301278 n/a–n/a.
[56] D.-W. Chung, M. Ebner, D.R. Ely, V. Wood, R.E. Garcia, Validity of the Bruggeman relation for porous electrodes, Model. Simul. Mater. Sci. Eng. 21 (2013), http://dx.doi.org/10.1088/0965-0393/21/7/074009.
[57] B. Tjaden, S.J. Cooper, D. Brett, D. Kramer, On the origin and application of the Bruggeman correlation for analysing transport phenomena in electrochemical systems, Curr. Opin. Chem. Eng. 12 (2016) 44–51, http://dx.doi.org/10.1016/j.coche.2016.02.006.
[58] I.V. Thorat, D.E. Stephenson, N.A. Zacharias, K. Zaghib, J.N. Harb, D.R. Wheeler, Quantifying tortuosity in porous Li-ion battery materials, J. Power Sources 188 (2009) 592–600, http://dx.doi.org/10.1016/j.jpowsour.2008.12.032.